LAWRENCE
LIVERMORE
NATIONAL
LABORATORY

UCRL-JRNL-201468

Breadboard Testing of a Phase Conjugate Engine with an Interferometric Wave-Front Sensor and a MEMS-Based Spatial Light Modulator

K.L. Baker, E.A. Stappaerts, D. Gavel, S.C. Wilks, J. Tucker, D.A. Silva, J. Olsen, S.S. Olivier, P.E. Young, M.W. Kartz, L.M. Flath, M. L. Minden, Oscar Azucena

December 15, 2003

Journal of the Optical Society of America A

Disclaimer

Breadboard Testing of a Phase Conjugate Engine with an Interferometric Wave-Front Sensor and a MEMS-Based Spatial Light Modulator

K.L. Baker, E.A. Stappaerts, S.C. Wilks, D. Gavel, J. Tucker, D.A. Silva, J. Olsen, S.S. Olivier, P.E. Young, M.W. Kartz, L.M. Flath, P. Kruelevitch, J. Crawford and Oscar Azucena
Lawrence Livermore National Laboratory, Livermore, CA 94550 USA

M. L. Minden(?)
Hughes Research Laboratories, Malibu, CA 90265 USA

P. Bierden(?)
Boston Micromachines Corporation, Watertown, MA 02472 USA

W.H. Long, Jr.(?)
Northrop Grumman Space Technology, Redondo Beach, CA 90278 USA

Abstract

Laboratory breadboard results of a high-speed adaptive optics system are presented. The wave-front sensor for the adaptive optics system is based on a quadrature interferometer, which directly measures the turbulence induced phase aberrations. The laboratory experiments were conducted using Kolmogorov phase screens to simulate atmospheric phase distortions with the characterization of these plates presented below. The spatial light modulator used in the phase conjugate engine was a MEMS-based piston-only correction device with 1024 actuators. The overall system achieved correction speeds in excess of 800 hz and Strehl ratios greater than 0.5 with the Kolmogorov phase screens.

OCIS codes: 010.1080, 010.7350, 120.2880, 090.1000

I. INTRODUCTION

Adaptive optics (AO) systems used in astronomy and vision applications typically utilize Shack-Hartmann wave-front sensors and to a much lesser degree curvature wave-front sensors.[1, 2] These sensors measure the gradient and Laplacian of the phase, respectively. These systems typically operate with broadband incoherent sources where interferometric techniques, which directly measure the phase, are more difficult to implement. Interferometers, which measure phase directly, have been implemented in AO systems [3, 4], however, these systems are required to run in closed-loop to achieve a high Strehl ratio since they only sense one interferogram and can therefore only uniquely assign a phase value from 0 to π radians for instance. More recently a prototype of the system described in this article was demonstrated using a visible laser and a liquid crystal spatial light modulator.[5] This prototype system allowed many of the system concepts to be tested, however, the speed was limited to ~1 hz due to the response time of the liquid crystal device. This article discusses a coherent light AO system based on a quadrature Twyman-Green interferometer that operates at a wavelength of 1.5 μm and achieves correction speeds of greater than 800 hz.[6] This wave-front sensor generates quadrature interferograms, allowing reconstruction of the wave-front over the range of 0 to 2π radians. The system operates in open-loop, where open-loop in this context means that the correction applied to the spatial-light-modulator in the previous pass through the loop is not sensed by the interferometer. Advantages of open-loop operation include increased correction bandwidth and reduced sensitivity to registration errors.

In section II, the experimental layout of the phase conjugate engine is presented along with a description of beam propagation through the system. The experimental

layout includes phase plates that are used to simulate the Kolmogorov turbulence spectrum expected from atmospheric propagation. Section III discusses how these phase plates were manufactured. Section IV then presents the characterization of these phase plates, which is required to quantitatively predict the performance of the system. Section V details the experimental characterization and wave optics simulations of the corrected Strehl ratios achieved with the system. A discussion on the results is also given in this section. These results are then summarized in the VI and final section.

II. EXPERIMENTAL LAYOUT

The optical layout of the IR laboratory breadboard system is shown in Figure 1. It consists primarily of an interferometric wave-front sensor, a MEMS-based spatial-light-modulator built by the Boston Micromachines Corporation (BMC), an Erbium-doped fiber laser built by HRL laboratories and computer hardware/software to analyze the wavefront and implement the phase correction. The system was designed for open-loop operation, however, a closed-loop arm exists such that the wave-front camera can be aligned precisely with the MEMS-based spatial light modulator and in fact either configuration can be used simply by blocking the remaining beam path. The laser source is an Erbium-doped fiber laser operating at 1530 nm. The laser has two independently triggerable arms, which output nearly transform-limited pulses of 1 ns duration and pulse energies of 7 μJ and 100 nJ for the probe beam and the reference beam, respectively.

Polarization optics are utilized in the testbed to form the two interferograms with a $\pi/2$ phase shift between them and also to control the relative signal levels in the arms of the interferometer. The linearly polarized output of the probe beam is rotated

approximately $\pi/4$ degrees from the vertical direction. The probe beam passes through three aberrating phase plates that were designed to simulate atmospheric turbulence with a Kolmogorov turbulence spectrum. After traversing the phase plates, the probe beam passes though a square aperture that is relay imaged onto both the MEMS-based spatial light modulator and the interferometric wave-front camera. The probe beam passes through the two lenses, used to form a conjugate image of the aperture onto the MEMS-based spatial light modulator. After passing through the second lens, the probe beam is incident upon a thin film polarizer, which passes the p-polarized component but reflects the s-polarized component. The p-polarized component passes through a second thin film polarizer and a quarter-wave plate before reaching the MEMS-based spatial light modulator. After reflection off of the MEMS-based spatial light modulator, the probe beam passes back through the quarter wave-plate and is incident upon the thin film polarizer. By double passing the quarter wave plate, the probe beam is rotated by ninety degrees and converted to an s-polarized beam that is then reflected from the thin film polarizer and directed toward the far-field camera. The beam passes through a 50/50 beamsplitter with the transmitted light going to the far-field camera and the reflected light forming the closed-loop arm of the wave-front sensor. The reflected light is then reflected by two more 50/50 beamsplitters where the s-polarized probe beam is then mixed with the reference beam when the system is set up for closed-loop operation. For open-loop operation, the s-polarized probe beam, reflected by the first thin film polarizer, passes through an optical trombone and two 50/50 beamsplitters before being combined with the reference beam. The reference beam is reflected off of a third thin film polarizer near the top of Figure 1 and the resulting s-polarized beam passes through a quarter wave plate

(QWP) at 45 degrees to vertical, which converts the linearly polarized light into circularly polarized light with the orthogonal polarizations 90 degrees out of phase with one another. After passing through the QWP, the reference and probe beams, in either the open or closed loop geometries, are combined using a non-polarizing 50/50 beamsplitter. Both beams then pass through a half wave plate that rotates their polarization by $\pi/4$, producing equal amplitude horizontal and vertical components of the probe beam while maintaining the $\pi/2$ phase shift between the horizontal and vertical components of the reference beam. The reference and probe beams then pass through a telescope. A Wollaston prism, at the focus of the first telescope lens, separates the two interferograms in angle. The two interferograms, having orthogonal polarizations, exit the Wollaston prism at an angle of approximately 1.93 degrees with respect to one another and are collimated by the two lens placed directly after the Wollaston prism. The two spatially separated interferograms are then directed to the IR camera, which is in a conjugate plane to the spatial light modulator and to the entrance aperture of the system.

III. PHASE PLATE CHARACTERIZATION

A set of three atmospheric phase screens, which can be seen in Figure 1, were designed and fabricated to test the performance of the AO system. These phase screens were designed to mimic a 0.75 km atmospheric propagation path. Three screens were chosen to provide a distribution of aberrations along the path, rather than having all of the aberrations on a single screen that would be more easily conjugated. Fabrication of the phase screens took place in the Microfabrication Laboratory at the Lawrence Livermore National Laboratory (LLNL). A design consisting of 16 phase levels was chosen for the

phase plates, which required four binary masks (2^4 = 16 levels.) The simulated phase profile for the masks was decomposed into these 4 binary masks, each with the binary etch depths required for the given the phase variation.

The ability of the phase conjugate engine to correct phase aberrations was tested in the laboratory using these phase plates to represent the atmospherically induced aberrations. These phase plates were designed to produce a Kolmogorov turbulence spectrum, thereby simulating atmospheric propagation. In order to test the system performance, the phase plates were first characterized on the IR system after they had been fabricated. Once the phase plate characterization was completed, a quantitative analysis of the phase conjugate engine was performed. The phase plates were mounted on a common axis such that the plates could be rotated transverse to the optical axis to simulate transverse wind velocity and to test the temporal performance of the phase conjugate engine.

The plates were first characterized by measuring the aberrated phase profile passing through the phase plates and subsequently unwrapping the phase. This task was accomplished by taking a large number of interferograms, ~3000, as the phase plates were rotated. The interferograms allowed the determination of the two-dimensional wrapped (modulo-2π) phase across the input aperture of the system. Before the parameters used to describe the turbulence spectrum could be determined, the phase had to be unwrapped. The phase was unwrapped using a minimum weighted discontinuity method.[7] This technique partitions the wrapped phase profile into two connected regions, separated by discontinuity curves. The algorithm then raises the phase in one of the regions by 2π thereby reducing the weighted sum of the discontinuities. This process is

repeated until no further partitioning is possible. An example of a wrapped phase determined from a single set of sine and cosine interferograms is shown in Figure 2(a) below. After processing the wrapped phase with the minimum weighted discontinuity algorithm, the unwrapped phase shown in Figure 2(b) was recovered. The unwrapped phase consists primarily of tilt, as expected from a Kolmogorov turbulence spectrum, and varies over 26 radians, or almost 4 waves.

Once the unwrapped phase has been recovered, the parameters and scaling relations used to describe the turbulence spectrum can be determined. One such scaling relation is the phase structure function, $D_\phi(r)$. The phase structure function is defined by $D_\phi(r) = <|\phi(x) - \phi(x+r)|^2>$, which for a Kolmogorov turbulence spectrum can be expressed analytically as $D_\phi(r) = 6.88(r/r_o)^{5/3}$. In this expression, r_o is the Fried parameter, which is also known as the transverse coherence length. The phase structure function is constructed by comparing the phase at a given location to the phase at an increasing distance from that location. The results from a single frame are shown in Figure 2(c). In this figure the gray line denotes the phase structure function determined from the experimentally measured phase across the aperture. The solid black line denotes an analytic fit to the structure function assuming a Kolmogorov turbulence spectrum and a Fried parameter of 1.3 mm. The slope of the experimentally determined structure function is in reasonably good agreement with the slope of the analytic fit indicating that the spectrum closely resembles a Kolmogorov turbulence spectrum. A median average over 3000 such structure functions, collected while the plates are rotating, is shown in Figure 3. Again there is a relatively good fit between the slopes of the experimentally averaged structure functions and the analytic structure function expected from a

Kolmogorov turbulence spectrum. In this case, the solid black line represents the experimentally measured data and the solid and dashed gray lines represents analytic Kolmogorov fits for a Fried parameter of 1.0 mm and 1.3 mm, respectively.

The Fried parameter, r_0, was also determined from a measurement of the point-spread function (PSF) given by the far-field image. In this case, 100 separate far-field images were taken as the phase plates were rotating. An example of a single frame, showing the speckle pattern produced in the far-field, is displayed in Figure 4(a). To evaluate the Fried parameter, the far-field patterns from 100 separate frames were added together, after registering their centroid to a common location. The averaged point-spread function is shown in Figure 4(b). By radially averaging the composite far-field pattern, a numerical fit to the point spread function can be determined. For a Kolmogorv turbulence spectrum, the short exposure point-spread function is given by the radial average of the Fourier transform of the product of the optical transfer function of the phase plates and the optical system. In the case of a short-exposure atmospheric transfer function, tip/tilt is removed. The analytical phase structure function is calculated similarly to the long-exposure phase structure function, however, a filter function is inserted within the integral to remove tip/tilt. The analytical optical transfer function of the atmosphere for a short exposure, assuming a Kolmogorov turbulence spectrum, is given by $\exp\{-(1-(r/D)^{1/3})D_\phi(r)/2\}$ or $\exp\{-3.44(r/r_o)^{5/3}(1-(r/D)^{1/3})\}$, where D represents the input aperture of the system and again $D_\phi(r) = 6.88(r/r_o)^{5/3}$ is the long-exposure phase structure function. The optical transfer functions are multiplied together and then the Fourier transform of this product is taken to obtain the numerically generated point-spread function. The radial average of this point-spread function is then compared to the experimentally measured

point spread function to determine the Fried parameter, r_o, which is the only free parameter. A comparison between the experimentally measured point spread function and the numerically fit point spread function for the summation of the 100 separate frames is shown in Figure 5. The gray line denotes the numerically determined point spread function for a short time exposure Kolmogorov turbulence spectrum assuming a Fried parameter of 1.1 mm. The black line denotes the radially averaged point spread function from the averaged experimentally measured far-fields. The Fried parameter estimate of 1.1 mm is very close to the fit to the structure function determined above.

The temporal power spectrum associated with the rotating phase plates was also measured to test the temporal delay error associated with the CCIT system. To perform this test, the phase plates were mounted on a common axis so that they could be rotated along the aperture plane. The projection of the 11.4 mm square aperture onto the rotating phase plates is shown in Figure 6. The center of the aperture is located 2.05 cm from the center of the Kolmogorov phase plates. The transverse velocity, v, of the phase plate is equal to the angular frequency, ω, in which the phase plates are spinning multiplied by the distance from the center, r, or $v=\omega r$. The angular frequency was measured in the laboratory to be $\omega=0.72V$ (rad/sec), where V is the voltage applied to the motor. The maximum velocity applied to the motor for the experiments was ~ 22 Volts which produced a maximum velocity of 42 cm/sec. Because the aperture extends over a range of distances from the axis, the transverse velocity of the plates varies across the aperture. The velocity ranges from $v=1.07V$ (cm/sec) at the inside edge of the aperture to $v=1.9V$ (cm/sec) at the outer edge of the aperture, where again V represents the voltage applied to the linear motor. The velocity at the center of the aperture is approximately $v=1.5V$

(cm/sec).

The temporal power spectrum was determined by analyzing the temporal dynamics of the phase. Again the 3000 interferograms were unwrapped as described previously to determine the phase across the aperture for each frame. The resulting phase as a function of time for each of the pixels could then be determined, given the 3000 frames collected at a frequency, f, of 580 hz. A representative plot of phase vs. time for a single pixel is shown below in Figure 7. To determine the temporal power spectrum, the open loop phase vs. time measurement for each of the (32x32) pixels was Fourier transformed. The square of the Fourier transformed phase vs. time was then summed over all of the pixels to determine the temporal power spectrum, $W_\phi(f)$. This process was then repeated for several different transverse velocities associated with the rotating phase plates. The results of this analysis are shown below in Figure 8. This figure represents the temporal power spectrum measured at four different voltages applied to the motors. The corresponding plate velocity at the center of the aperture is given in each of the four frames and ranges from v=0.75 cm/sec in Figure 8(a) to v=7.5 cm/sec in Figure 8(d). Each of these figures has the experimentally determined temporal power spectrum, displayed as a black line, and an analytical line representing the temporal power spectrum associated with a Kolmogorov spectrum, $W_\phi(f)$, displayed as a gray line. The analytic fit uses a value of r_o=1.3 mm and the velocity at the center of the aperture, calculated from the expression v=1.5V as discussed in the previous paragraph. The analytical expression used to fit the experimental data uses the expression $W_\phi(f)=\pi^{-1}(F_g)^{5/3}f^{-8/3}$, where F_g is the Greenwood frequency. In our case where the plates are moving at the same velocity along the propagation distance, the Greenwood frequency can be expressed as F_g

~$0.43v_{\perp}/r_0$, where $v_{\perp}$ represents the transverse velocity of the phase plates and r_o is the Fried parameter. The phase plates exhibit the proper frequency scaling, $f^{-8/3}$, over nearly three decades. The spectrum exhibits a roll-off at low frequencies which is consistent with a Von Karman type spectrum and a reasonable fit to a Von Karman spectrum, $W_{\varphi}(f)_{V\_K}=(\pi)^{-1}f_g^{5/3}|f^2+(\kappa_o v_{\perp}/2\pi)^2|^{-4/3}$, is achieved with κ_o~3.5 cm. The high frequency pedestal is due to the finite pixel size of the detector. The phase plates rotate across a given pixel, at the center of the aperture, at a rate of $f_c=v/d=\{1.5V$ (cm/sec)$\}/\{1.14$ (cm)/32 (pix/aperture)$\}$, where d is the individual pixel size on the aperture. For a voltage of five volts, V=5, applied to the motors, as in 8(d), the frequency at which a given point on the phase plate rotates across a pixel is f_c=210 hz. The Nyquist theorem states that for a frequency to be resolvable, the wavelength must be sampled at greater than twice its frequency. This is in good agreement with the frequency at which the noise floor begins in Figure 8(d). There is a proportional decrease in the onset of the noise floor as the velocity is decreased in Figures 8(a-c).

IV. EXPERIMENTAL RESULTS

Once the phase plates were characterized, then the system performance was quantified, primarily by determining the Strehl ratio. The Strehl ratio was calculated by measuring both the point-spread function (PSF) with a far-field camera and the near-field image of the probe beam with the wave-front camera. With these two measurements, the Strehl ratio was calculated and compared with the expected phase variances associated with a Kolmogorov turbulence spectrum. The near-field image of the probe beam after transmission through the phase plates, was measured at the wave-front camera, which is

in a conjugate image plane to the input aperture of the system. The near-field image, displayed in Figure 9, was taken by temporarily blocking the reference beam. Using the far-field camera, the PSF was recorded as the CCIT phase conjugate engine was correcting the wave-front. The measured PSF, for the case where the phase plates had a transverse velocity of v=1.5 cm/sec, is shown in Figure 10 (b). The ideal PSF, shown in Figure 10 (a), was found by Fourier transforming the near-field image from Figure 9 and normalizing the signal level to that obtained from the measured PSF presented in 10 (b). Figure 10 (c) and (d) represent lineouts through the center of the ideal PSF, gray line, and the measured PSF, black line, in the horizontal and vertical directions, respectively. A sequence of 100 such PSFs were measured for several different transverse velocities. The absolute strehl ratios from these measurements are shown in Figure 11 below. This figure represents the instantaneous Strehl ratios obtained for five distinct velocities while the phase conjugate engine was correcting the wave-front and also the uncorrected Strehl ratio.

The instantaneous Strehl ratios, for the lowest velocity, shown in Figure 11 was averaged over the 100 separate frames to examine the fitting error associated with the CCIT phase conjugate engine. The resultant averaged Strehl ratio in this case was S_r=0.55 at the slowest phase plate speed of v=0.75 cm/sec. The strehl ratio due to the fitting error for a Kolmogorov turbulence spectrum is given by the expression $S_r=\exp\{-1.3(d/r_o)^{5/3}\}$, for a square aperture, where d is the sub-aperture size. For the laboratory demonstration, the sub-aperture size is approximately 11.4/32 or 356 μm. The expected Strehl ratio from fitting error in this case would be $S_r \sim 0.84$, which is slightly higher than the measured Strehl ratio of S_r=0.55. The MEMS-based spatial light modulator, which

consisted of 32x32 pixels, in the phase conjugate engine had approximately 60 bad pixels and the outer actuators were not activated giving nearly 18% of the actuators that were not contributing to the correction. Wave optics simulations performed using a bad pixel map of the actuators indicated that the non-activated pixels caused a reduction in the Strehl ratio of approximately 22 %. This gave an estimated maximum Strehl achievable of approximately $S_r=(1.0-0.22)*\exp\{-1.3(d/r_o)^{5/3}\}$ or $S_r\sim0.66$. The maximum achievable Strehl is also reduced by the 3-bit algorithm[8,9] used to determine the phase which also lowers the Strehl ratio by a factor of 0.95 to $S_r\sim0.95*0.66 = 0.63$, which is within approximately 15 % of the measured average Strehl ratio.

The instantaneous Strehl ratios shown in Figure 11 can then be averaged over the 100 separate frames for each of the velocities to examine the time delay error associated with the CCIT phase conjugate engine. The time delay error arises because of the finite time between measurement of the aberrated wave-front and application of the correction to the MEMS device. During this time delay, the high frequency components of the atmosphere undergo a significant change and the system is unable to correct the highest turbulence frequencies. The time delay, τ, is the time between when the probe beam samples the atmosphere and when the correction has been applied to the spatial light modulator, which in the case of the CCIT system was generally 1/580 hz or 1.72 ms. The resultant averaged Strehl ratio for each of the transverse plate velocities is displayed as the black line in Figure 12. This experimentally determined Strehl ratio was then fit to the analytical Strehl ratio for a Kolmogorov turbulence spectrum, $\exp\{-6.88(v\tau/r_o)^{5/3}\}$, normalized to the Strehl ratio obtained when the phase plates are stationary. A very good fit is obtained with $r_o=1.1$ mm, again in agreement with the previous measurements.

V. SUMMARY

In the laboratory, the phase conjugate engine achieved large improvements over the uncorrected, non-tip-tilt corrected PSF resulting from propagation through the phase plates. This can be seen in Figure 13 which displays the measured point-spread function for the CCIT system when the system is uncorrected and corrected, respectively. Figure 12 indicates a corrected average Strehl ratio of S_r=0.55 at the slowest phase plate speed of v=0.75 cm/sec and an uncorrected Strehl ratio of S_r=0.01 without tip/tilt correction. The measured uncorrected Strehl ratio of S_r=0.01 is in good agreement with the expected Strehl ratio of $S_r=(r_o/D)^2=(1.2\text{ mm}/11.4\text{ mm})^2=0.011$.

Acknowledgements

The authors would like to acknowledge H. Komine for suggesting a Wollaston prism, in the configuration shown in Figure 1, for channel separation on the CCD camera and L. Pleasance his design for a variable focal length lens combination. This effort was sponsored by the Defense Advanced Research Projects Agency (DARPA) for work on the Coherent Communications, Imaging and Targeting (CCIT) program, 02-L493. This work was performed under the auspices of the U.S. Department of Energy by the University of California, Lawrence Livermore National Laboratory under contract No. W-7405-Eng-48.

REFERENCES

[1] J. W. Hardy, *Adaptive Optics for Astronomical Telescopes* (Oxford University Press, Oxford, 1998).

[2] R. K. Tyson, *Principles of Adaptive Optics* (Academic Press, Boston, 1998).

[3] R. Dou and M. K. Giles, "Closed-loop adaptive-optics system with a liquid-crystal television as a phase retarder," Opt. Lett. **20**, 1583 (1995).

[4] T. Shirai, T. H. Barnes, and T. G. Haskell, "Adaptive wave-front correction by means of all-optical feedback interferometry," Opt. Lett. **25**, 773 (2000).

[5] K. L. Baker, E. A. Stappaerts, S. C. Wilks, et al., "Open and Closed-Loop Aberration Correction using a Quadrature Interferometric Wave-Front Sensor," Optics Letters (Dec. 2003).

[6] C. J. Buchenauer and A. R. Jacobson, "Quadrature Interferometer for plasma density measurements," Rev. Sci. Instrum. **48**, 769 (1977).

[7] T. J. Flynn, "Two-dimensional phase unwrapping with minimum weighted discontinuity," JOSA A **14**, 2692 (1997).

[8] G. D. Love, N. Andrews, P. Burch, et al., "Binary adaptive optics: atmospheric wave-front correction with a half-wave phase shifter," Applied Optics **34**, 6058 (1995).

[9] K. L. Baker, E. A. Stappaerts, S. C. Wilks, et al., "Performance of a phase-conjugate-engine implementing a finite-bit phase correction," Optics Letters (submitted Nov. 2003).

10 FIGURE CAPTIONS

Figure 1 Laboratory breadboard setup used to test the performance of the phase conjugate engine in a controlled laboratory environment. The abbreviations stand for the following: BS, beam splitters; M, mirrors; L, lenses; S, shutters; A, apertures; TFP, thin film polarizers; $\lambda/2$ and $\lambda/4$, half and quarter wave-plates, respectively.

Figure 2 Phase profile across the aperture of the probe beam passing through the three phase plates. This particular phase profile was determined from a single set of sine and cosine interferograms. The wrapped and unwrapped phases and the resultant structure function are displayed in 2a, 2b and 2c, respectively.

Figure 3 Phase structure function averaged over 3000 separate phase structure functions. The 3000 phase structure functions were calculated from the wrapped phases determined from 3000 sets of sine and cosine interferograms.

Figure 4 Point spread functions measured with the aberrating phase plates rotating.

Figure 5 Fit to the radially averaged point spread function. The gray line denotes the numerically determined point spread function for a short time exposure Kolmogorov turbulence spectrum. The black line denotes the radially averaged point spread function from the averaged experimentally measured far-fields.

Figure 6 Phase plate geometry showing the 11.4 mm projection of the aperture on the phase plate.

Figure 7 Phase as a function of time for a single pixel on the wave-front camera.

Figure 8 Temporal power spectrum for four separate voltages applied to the phase plates. The resulting velocities, at the center of the apertures, are listed in each of the Figures. The experimentally determined temporal power spectrum is displayed as the black line in each of the graphs and an analytical Kolmogorov fit is displayed as a gray line as well. In each of these graphs, the analytical fits used a Fried parameter of r_o=1.3 mm and the transverse plate velocity in the exact center of the aperture.

Figure 9 Near-Field image of the probe beam after propagation through the phase plates as recorded on the wave-front camera.

Figure 10 Point-spread-functions used to determine the Strehl ratio. Figure 10 (b) represents the measured point spread function and Figure 10 (a) represents the ideal point spread function, given the near-field image shown in Figure 9 and the total energy measured in Figure 10 (b). Figure 10 (c-d) represent lineouts through the center of the point-spread-function for the ideal PSF, gray line, and the measured PSF, black line, in the horizontal and vertical directions, respectively.

Figure 11 Absolute Strehl ratios for 100 separate time taken as the phase plates are rotated. The different lines specified represent different transverse velocities at the center of the aperture

Figure 12 Absolute Strehl ratios averaged over 100 separate frames. The experimental data is represented by the black line and a fit to the data assuming a Kolmogorov turbulence spectrum is given by the gray line. The error bars denote the standard deviation of the Strehl ratios, over 100 images, displayed in Figure 11.

Figure 13 Point-spread-functions for the uncorrected and correct probe beams after propagation through the phase plates.

FIGURES

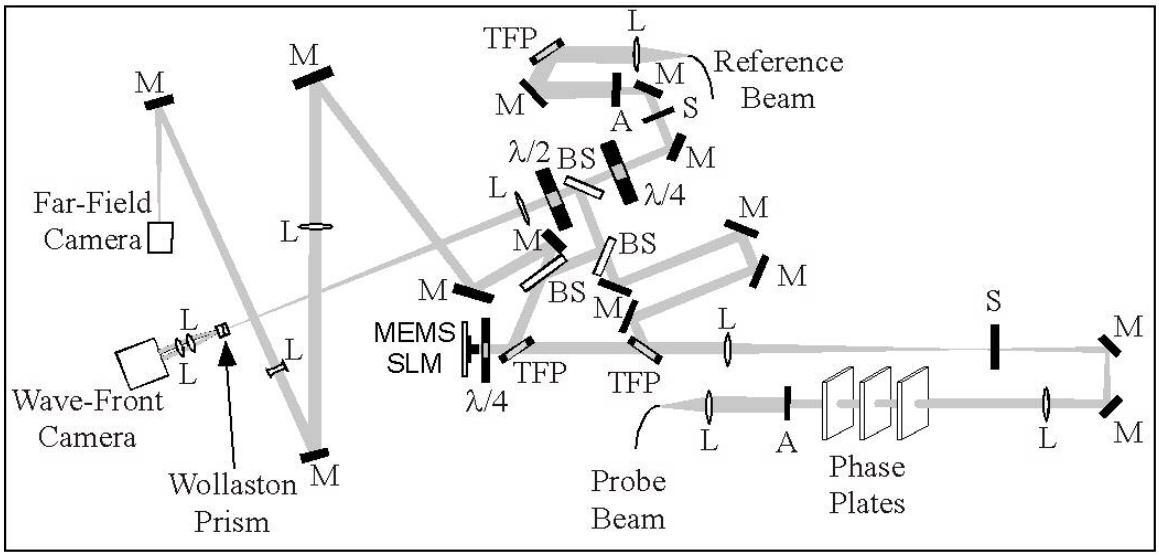

Figure 1

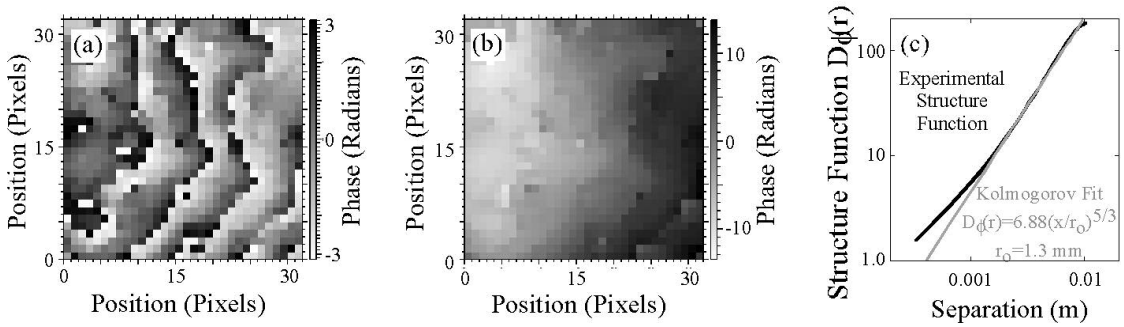
(a)
Position (Pixels)
Position (Pixels)
Phase (Radians)
3
0
-3
(b)
Position (Pixels)
Position (Pixels)
Phase (Radians)
10
0
-10
(c)
Experimental
Structure
Function
Kolmogorov Fit
$D_\phi(r)=6.88(x/r_o)^{5/3}$
r_o=1.3 mm
Structure Function $D_\phi(r)$
Separation (m)
100
10
1.0
0.001
0.01

Figure 2

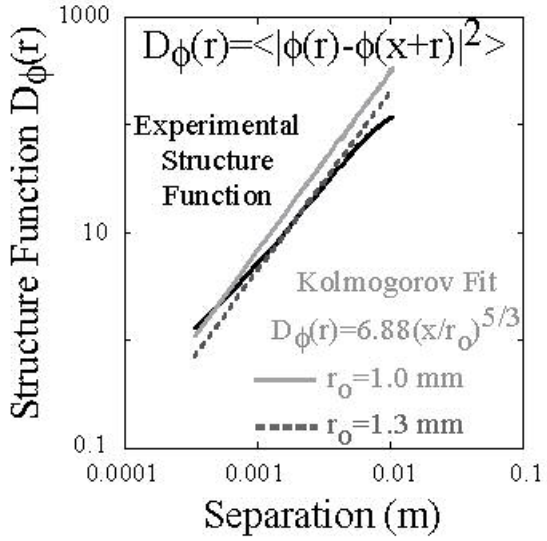
1000
10
0.1
0.0001
0.001
0.01
0.1
Structure Function $D_\phi(r)$
Separation (m)
$D_\phi(r)=<|\phi(r)-\phi(x+r)|^2>$
Experimental
Structure
Function
Kolmogorov Fit
$D_\phi(r)=6.88(x/r_o)^{5/3}$
r_o=1.0 mm
r_o=1.3 mm

Figure 3

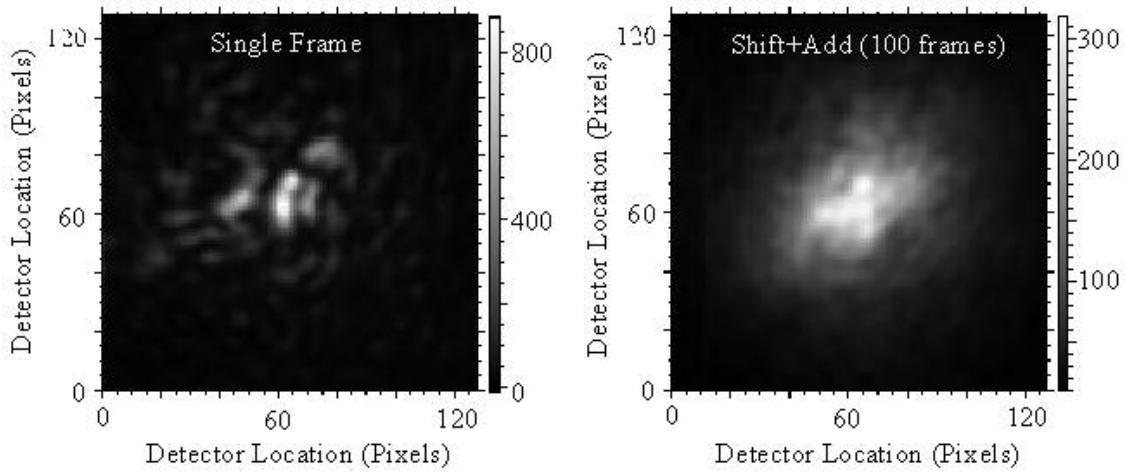
Single Frame
Shift+Add (100 frames)
Detector Location (Pixels)
Detector Location (Pixels)
0
60
120
800
400
300
200
100

Figure 4

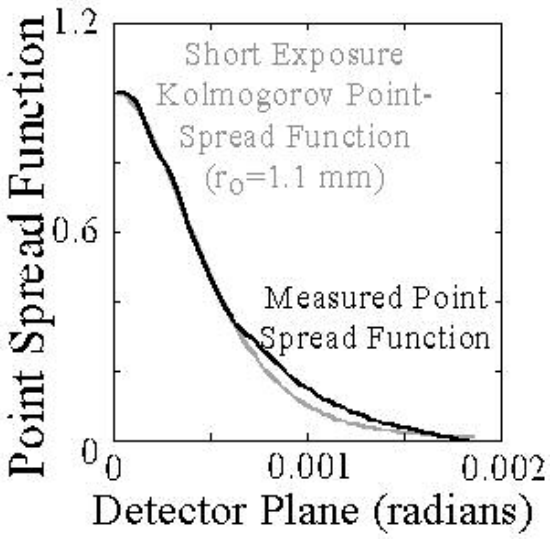
Point Spread Function
1.2
0.6
0
0
0.001
0.002
Detector Plane (radians)
Short Exposure
Kolmogorov Point-
Spread Function
(r_0=1.1 mm)
Measured Point
Spread Function

Figure 5

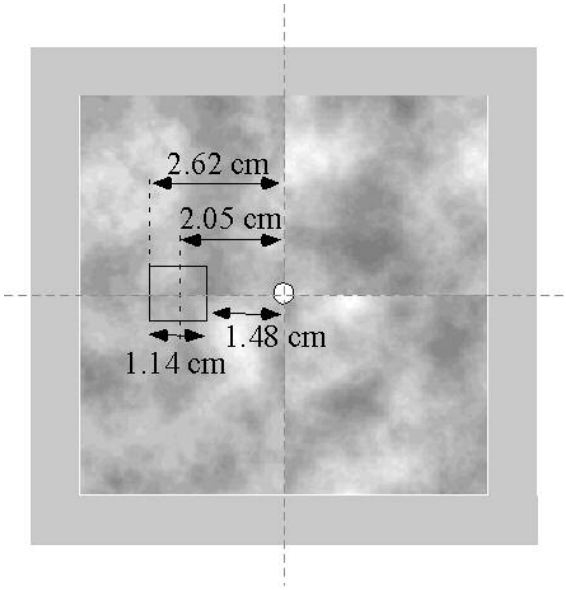

Figure 6

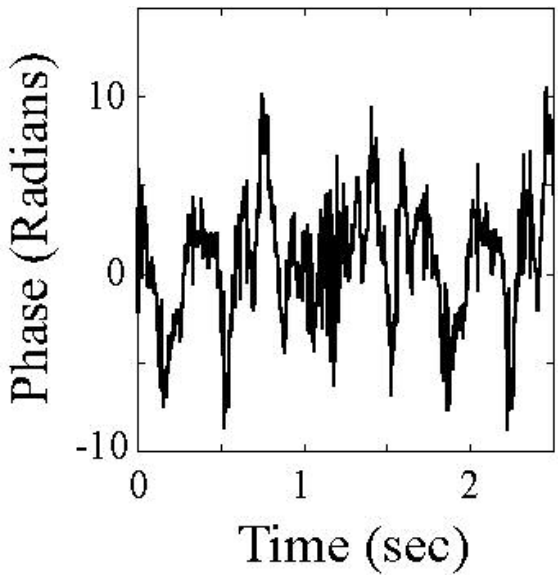

Figure 7

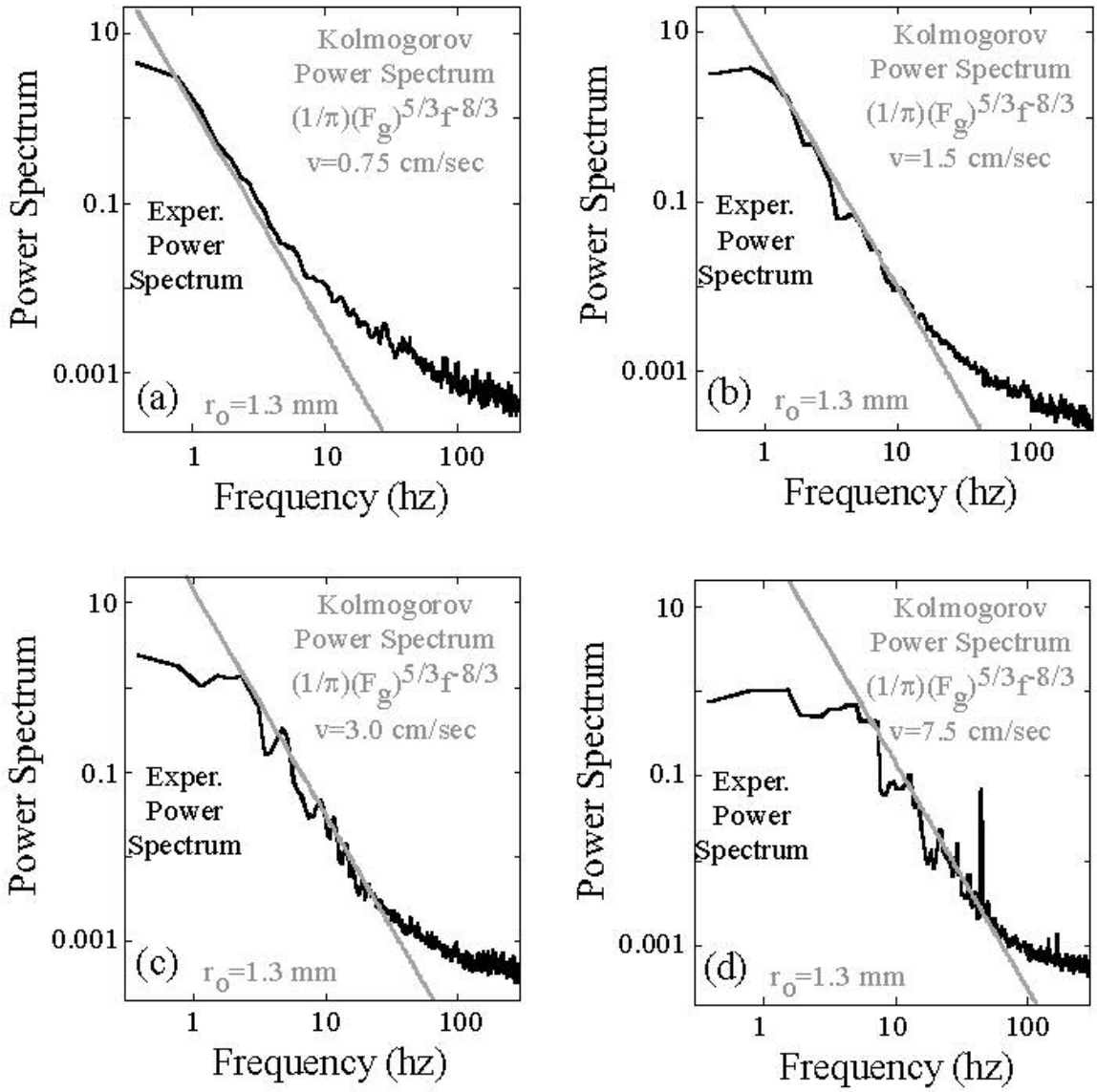
Power Spectrum
Frequency (hz)
Kolmogorov
Power Spectrum
$(1/\pi)(F_g)^{5/3}f^{-8/3}$
v=0.75 cm/sec
Exper.
Power
Spectrum
(a)
r_o=1.3 mm
v=1.5 cm/sec
(b)
v=3.0 cm/sec
(c)
v=7.5 cm/sec
(d)
10
0.1
0.001
1
10
100

Figure 8

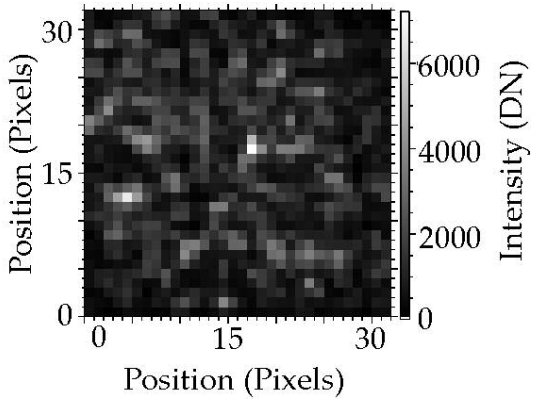
30
15
0
Position (Pixels)
0
15
30
Position (Pixels)
6000
4000
2000
0
Intensity (DN)

Figure 9

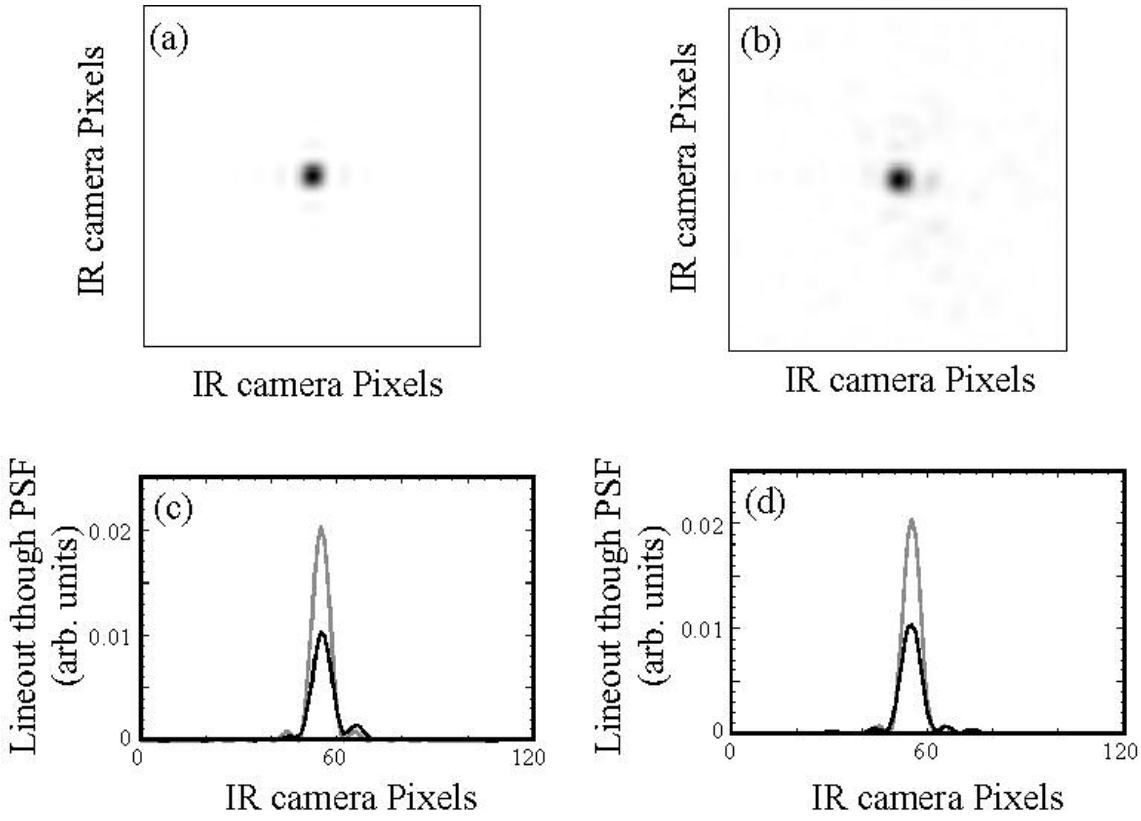
(a)
IR camera Pixels
IR camera Pixels
(b)
IR camera Pixels
IR camera Pixels
(c)
Lineout though PSF (arb. units)
0.02
0.01
0
0
60
120
IR camera Pixels
(d)
Lineout though PSF (arb. units)
0.02
0.01
0
0
60
120
IR camera Pixels

Figure 10

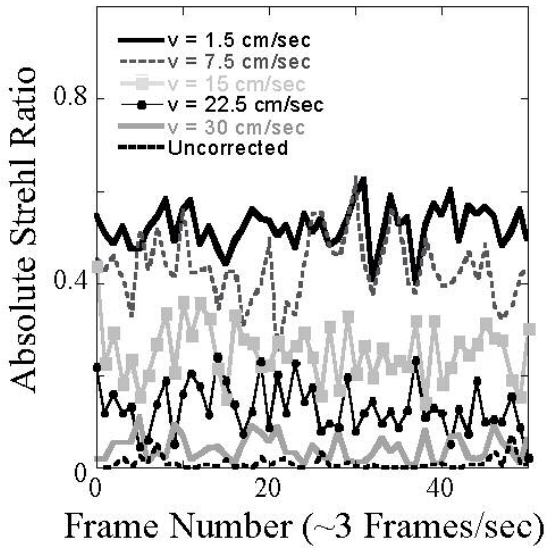
v = 1.5 cm/sec
v = 7.5 cm/sec
v = 15 cm/sec
v = 22.5 cm/sec
v = 30 cm/sec
Uncorrected
Absolute Strehl Ratio
0.8
0.4
0
0
20
40
Frame Number (~3 Frames/sec)

Figure 11

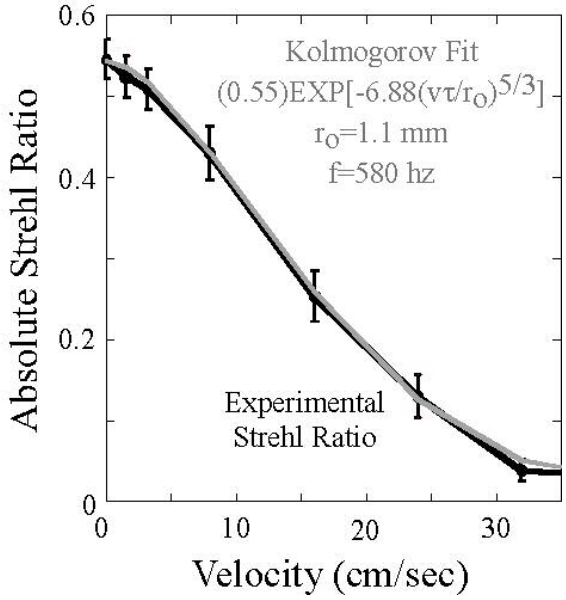
Absolute Strehl Ratio
0.6
0.4
0.2
0
0
10
20
30
Velocity (cm/sec)
Kolmogorov Fit
(0.55)EXP[-6.88(vτ/r0)5/3]
r0=1.1 mm
f=580 hz
Experimental
Strehl Ratio

Figure 12

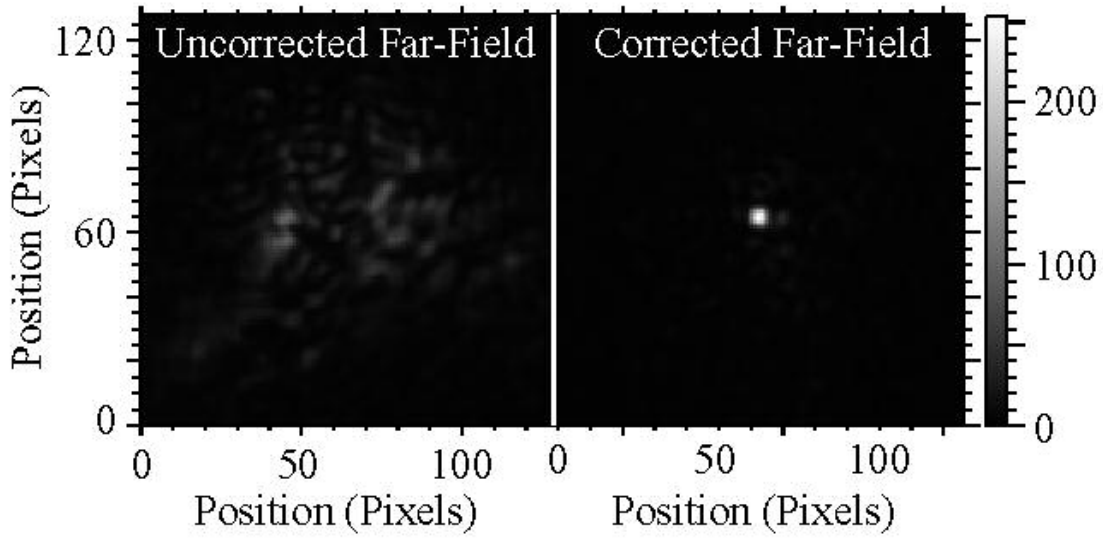
Uncorrected Far-Field
Corrected Far-Field
120
60
0
Position (Pixels)
0
50
100
Position (Pixels)
0
50
100
Position (Pixels)
200
100
0

Figure 13

University of California
Lawrence Livermore National Laboratory
Technical Information Department
Livermore, CA 94551